Casting of Tin Bronze Alloy in a Low-Head Mold

Mainul Hasan[*] and Latifa Begum

*Department of Mining & Materials Engineering, McGill University, M. H. Wong Building, 3610 University Street
Montreal, QC, Canada H3A 0C5*

Abstract

A computational modeling study has been carried out for a vertical Direct Chill (DC) ingot caster for tin bronze alloy (C903). The industrial caster modeled here consists of a low-head hot-top mold. The 3-D model incorporated the coupled laminar melt flow and wide mushy region solidification aspects of the casting process. The melt is delivered through the entire open top cross-section of the caster and, as a result, the inlet melt flow to the caster is equal to the casting speed. In confirmatory with the industry practice, three different cooling water temperatures, namely 10, 20 and 30°C, respectively, for the mold, impingement, and streaming regions have been considered. A verified in-house 3-D CFD code developed particularly for the DC casting process is used to investigate the effects of the major parameters such as casting speed ranging from 40 to 80 mm/min., inlet melt superheat varying from 16 to 64°C and the imposed mold-metal contact effective heat transfer coefficient changing from 1,500 to 4,500 W/(m²K) on the low-head casting process. The results are presented pictorially in the form of temperature and velocity fields. At the center of the ingot, the predicted results show that the sump depth, liquid depth, and mushy thickness increase linearly with the casting speed. The shell thickness at the exit of the mold decreases linearly with the casting speed. Useful, practical correlations concerning the above quantities with casting speed are provided to facilitate designing such casters for bronze.

Keywords: *low-head DC casting; 3-D modeling; tin bronze alloy (C903); mushy zone; variable water cooling conditions.*

Nomenclature

A^*	Darcy coefficient	f_s	solid fraction
a_p, a_{nb}	coefficients in the discretized governing equations	G^*	production term in turbulent kinetic energy equation
b	discretized source term	Gr	Grashof number
c_1, c_2, c_μ	empirical constants in low Reynolds number model	Gr_m	modified Grashof number (Gr/Ste)
c_P	specific heat	g_x	gravitational acceleration in the x-direction
C	morphology constant	h	sensible heat
D	hydraulic diameter of the caster (the entire cross-section of the ingot)	h_∞	ambient enthalpy
		H	total heat (sensible and latent)
D_k^*	extra dissipation term in k-equation	k	turbulent kinetic energy
E_ε^*	extra generation term in ε-equation	K	thermal conductivity of aluminum (solid or liquid)
f_1, f_2, f_μ	empirical constants used in low-Re version of k-ϵ models	P	hydrodynamic pressure
		Pe	Peclet number [non-dimensional]
f_l	liquid fraction	Pr	laminar Prandtl number

* Corresponding author

Re	Reynolds number
Re_t	turbulent Reynolds number based on the turbulent quantities
S	source term
S_Φ	source term associated with Φ
$S_k{}^*$	non-dimensional source term associated with buoyancy term in k-equation
$S_\varepsilon{}^*$	non-dimensional source term associated with buoyancy term in ε-equation
Ste	Stefan number
T	temperature T_{in} inlet temperature
T_l	liquidus temperature
T_s	solidus temperature
T_{surf}	slab surface temperature
u_i	velocity component in the *i-th* direction; corresponding to u
$\bar{u}_i$	time-average velocity component in the *i-th* direction
u_{in}	inlet velocity
u_s	casting speed
U, V, W	non-dimensional form of the u, v and w velocities
U_s	non-dimensional form of u_s
x	axial direction
y	horizontal direction parallel to the wide face

z	horizontal direction parallel to the narrow face
X, Y, Z	non-dimensional form of x, y, z
i, j, k	coordinate direction

Greek symbols

ΔH	nodal latent heat
ΔH_f	latent heat of solidification
Γ_Φ	diffusion coefficient associated with
ρ	alloy density
μ_l	laminar viscosity
μ_t	turbulent viscosity or eddy diffusivity
v	laminar kinematic viscosity
Φ	generalized dependent variable
Γ_{eff}	effective diffusivity
ϵ	rate of energy dissipation
ϵ_{in}	inlet rate of energy dissipation
γ	effective convective heat transfer coefficient
$\sigma_k , \sigma_\epsilon$	turbulence model constants
σ_t	turbulent Prandtl number

Superscripts

$*$	non-dimensional variables
–	time-averaged variables

Subscripts

P	center of the grid point
nb	neighbor of grid point P

1. Introduction

Among the various metallic alloys, the tin bronze alloy is one of the oldest alloys of copper and tin used my mankind. The percentage of tin in this alloy varies between 7.5 to 9.0 wt%. A low tin content makes the alloy softer while a high tin content makes the bronze alloy harder. This alloy is hard and strong and is most often used in high-load, low-speed applications. For making smaller objects, this alloy is cast by die casting, sand casting, permanent mold casting, investment casting, etc. If the objective is to make good quality casts, particularly in larger sizes, the above casting methods are not suitable since they make poor quality casts with a number of unacceptable internal defects. In producing industrial sizes and rates of better quality casts of non-ferrous alloys in an economical way, the semi-continuous vertical direct chill casting (DCC) process has been found to be more suitable [1]. The DCC process is in fact, nowadays the predominant route for casting of non-ferrous metals and their alloys such as aluminum, magnesium, copper, zinc, etc. The advantages of this process lie in the fact that it is quite flexible and versatile. Because of the extensive industrial usages, the description of the DCC process is quite well documented in a number of recent books and studies [1-2], including in the recent publications of the present authors [3-8]. To acquaint the general readers about the DCC process, a brief description of the process is given below.

The casting in a DCC process starts with a bottomless mold which is initially kept plugged by a retractable bottom block. The mold-bottom block assembly, thus forms a mold cavity. The mold

cavity is then filled from the top with the melt to be cast up to a predetermined height using a suitable melt distributor. In order to solidify the incoming melt, its superheat has to be removed. This is done by circulating chilled water through the inner channels of the mold. The flow rate and the temperature of the circulating water are carefully controlled so that the inner faces of the mold remain at a temperature much below the solidus temperature of the melt during the total casting time. Because of the heat extraction by the cooling water through the mold walls, and embryonic solid shell is developed on the inner faces of the mold walls. After a small time break, the bottom block holding the partially solidified ingot is slowly lowered by the hydraulic ram fitted at the bottom of the block. The downward speed of the block-ingot assembly is then gradually increased to reach the predetermined casting speed. As the ingot exits the mold, it is cooled further by the impinging water jets coming out of the holes at the bottom of the mold. In practice, the same circulating cooling water in the mold is used for the above purpose. The cooling that takes place in the mold region is inappropriately termed by the DCC industry as 'primary cooling' where only 5-10% of the total heat content of the incoming melt is usually removed. The cooling of the partially solidified ingot that takes place below the exit of the mold is termed 'secondary' cooling where 90 to 95% of the heat content of the ingot is removed [1]. It is very important that sufficient cooling of the melt in the mold takes place such that the metal does not come out at the exit of the mold in the liquid state. If the latter condition occurs, what is termed 'bleed-out' or 'run-out' condition, an explosion can occur and this may lead to a catastrophic and fatal condition in the casting plant.

The DCC process is initially unsteady and it is difficult to model the initial casting phase of the process because of the three-dimensional transient free-surface characteristic of the problem. Depending upon the aspect ratio of the ingot, casting speed, superheat, water cooling rates and water temperature, and the thermo-physical properties of the molten alloy, after about 0.5 m to 1.0 m length, the casting process reaches a pseudo-steady state [9]. Usually, after the casting of about 8 to 10 m in length, the melt delivery to the mold is stopped and the casting is suspended. From the water casting pit the cast is then taken away for homogenization, and for hot and cold rolling to obtain a plate/sheet/foil/strip of required thickness for various useful applications.

As mentioned above, apart from the prevention of the bleed-out condition, the initial cooling of the melt by the chilled mold wall is also critical since it dictates the development of the initial ingot shell as well as the microstructure and surface quality of the cast. Because of intense cooling of the semi-solid ingot by the water spray jets below the mold, the solid shell in the mold experiences thermal contraction and if the shell that has formed in the mold is not sufficiently strong enough, then it pulls out of the mold wall and thus an air gap between the solid shell and the mold wall is formed. The formation of the air gap leads to a drastic decrease in the heat transfer rate from the ingot to the mold, and this causes reheating of the shell due the internal heat transfer. If the extent of reheating is high, the solid shell could become semi-solid and could promote a number of uncontrollable internal and external casting defects such as cold shuts, drag marks, segregation knot, bleed-out, surface cracks and mixed fine/coarse microstructure [9].

Once the above defects appear on the cast surface, the surface and subsurface layers of the ingots need to be 'scalped' (the mechanical removal of the surface layer) before further processing. The process of scalping is tedious, time-consuming and expensive, which also results in the loss of material and productivity. Hence, much of research efforts in designing new DCC molds are geared towards the intention of eliminating the reheating of the shell in the mold by reducing mold cooling. In this regard, the casting company Wagstaff, Inc. (Spokane Valley, WA 99206,

USA), a major supplier of DC casting machines, has developed a low head composite (LHC) ingot casting technology which the company now markets all over the world under the name 'LHC[TM]' [10]. The essential difference between the conventional and LHC mold is that the active mold length in a conventional mold as stated earlier is usually between 70 to 80 mm while it is usually between 25 to 30 mm in LHC mold. As a result, no air gap forms in the latter mold. The quality of the cast in a low-head mold has been found to be much superior compared to the conventional DCC mold. Other benefits of the former mold is that it diminishes scalp rates, affords higher casting speeds; leads to a longer mold life, yields superior surface quality casts, reduces mold cooling water treatment costs, and provides safer operations [10].

Although the DCC process for aluminum alloys is a well-established process, very little modeling work exists in the literature, particularly for an industrial scale slab caster for bronze. A hot-top LHDC caster mold with an open top melt feeding system is modeled here. The melt is considered to have been supplied at an uniform temperature and velocity along the entire top cross-section of the mold. Fully elliptic 3-D laminar momentum and energy equations are used to model the macroscopic solidification aspects of the process. An in-house developed and well-verified CFD code is extended to model this casting problem. To the best of the knowledge of the authors an industrial size, low-head DC slab caster has not been previously modeled considering the coupled 3-D flow and solidification heat transfer aspect for bronze or in fact for any alloys of copper.

2. Mathematical Model

The studied physical model and the computational domain (yellow color region) considered is schematically shown in Figure 1. As the problem has a two-fold symmetry, to reduce the computational time, only an upper left-hand quarter of the physical domain was considered for the simulations. The computational domain is a rectangular parallelepiped and has a dimension of 2500 mm $\times$ 865 mm $\times$ 330 mm in x, y, and z directions, respectively. The origin of the coordinates of the computational domain is selected at the center of the physical domain at the top surface. The melt is considered to have been delivered in the direction of gravity at the top free-surface with a uniform velocity across the entire cross-section of the caster. The solid shell once formed in the mold it is then shifted downward at a preselected but constant casting speed during the steady state operation of the vertical DC casting process.

2.1. Test Material

The tin bronze (C903) alloy having a freezing range of 146°C was selected as a test material. The nominal chemical composition limits and the thermo-physical properties of this alloy are listed in Table 1 [11[1]] and Table 2 [11[2]], respectively. The tin bronze is a copper alloy in which the weight percentage of tin (Sn) usually varies from 7.5 to 9.0 %. Other predominant alloying elements in this alloy are Zinc (3.5 wt. %) and Nickel (1.0 wt. % max.). This alloy has many favorable properties which include good corrosion resistance, high wear resistance, moderate machinability, and remarkable hardness. Because of the aforementioned properties, this alloy is widely used in many useful applications. The cast products of this copper alloy are used in plumbing fixtures, marine fittings, portable water devices, valves, gears, pump components, etc. [12-13].
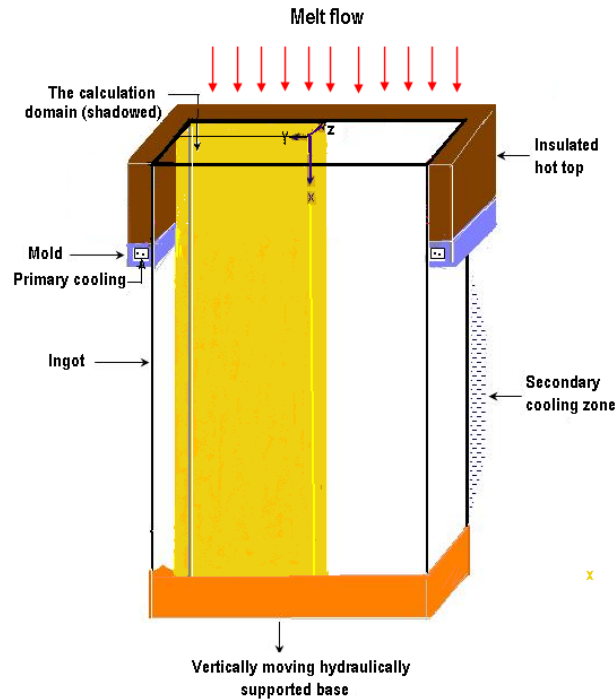
Figure 1. Schematic of the low-head DC caster and the computational domain for an open-top melt feeding scheme.

Table 1. Chemical composition limits of C 903 Tin Bronze[11].

Weight%	Cu	Sn	Ni	Pb	Zn	Sb	Fe	P	S	Al	Si
C 903 Tin Bronze	Balance 86.0 - 89.0	7.5 – 9.0	1.00 max.	0.30 max.	3.0 – 5.0	0.20 max.	0.20 max.	1.50 max.	0.05 max.	0.005 max.	0.005 max.

Table 2. Thermo-physical properties of Bronze[11].

Variable (unit)	Value
Thermal conductivity (liquid or solid) (kW/mK)	0.0748
Specific heat (liquid or solid) (kJ/kg $\times$ K)	0.3771
Latent heat of fusion (kJ/kg)	204.8
Liquidus temperature (°C)	1000.0
Solidus temperature (°C)	854.0
Viscosity (kg/m $\times$ s)	0.0044
Density (liquid or solid) (kg/m^3)	8800
Coefficient of thermal expansion at 20-200°C (/°C)	18.0×10^{-6}

2.2. Assumptions and Simplifications

To realistically model the casting problem some standard assumptions have been considered. Since all of the assumptions used here are provided in [12], hence to avoid duplications those assumptions are not listed here.

2.3. Numerical Procedure

2.3.1. Governing Equations for Laminar Melt Velocity and Enthalpy

The 3-D general transport equations for laminar melt velocity and enthalpy at steady state in Cartesian tensor notation can be written as follows.

$$\frac{\partial(\rho u_i \Phi)}{\partial x_i} = \frac{\partial}{\partial x_i}\left(\Gamma_\Phi \frac{\partial \Phi}{\partial x_i}\right) + S_\Phi \tag{1}$$

where, ρ, u_i, Γ_Φ and S_Φ are representing the melt density, the velocity component in the x_i - direction, the effective diffusion coefficient of Φ and the source term of Φ, respectively. Φ is equal to 1 for the continuity equation. For momentum equations, it is the velocity components u_i, while for the energy equation it represents the temperature T. The positive x-direction is taken parallel to the direction of the gravity field. The detailed derivation of the above general transport equation can be found in [14].

2.3.2. Solidification Modeling and Modeling of Fluid Flow in the Mushy Region

A single domain modeling approach was considered in the present study to model the mushy-region solidification problem since it does not require the tracking of the unknown interfaces (liquid-mushy and mushy-solid). The popular enthalpy-porosity method was implemented here [14-16]. One major advantage of this method is that, a single set of transport equations is able to appropriately handle all three regions namely, liquid, mushy, and solid zones. In this method, the total enthalpy is decomposed into sensible and nodal latent heat components in the energy equation

$$H = h + \Delta H \tag{2}$$

where h is the sensible heat, which is defined as

$$\int_{h_{ref}}^{h} dh = \int_{T_{ref}}^{T} c_p\, dT \tag{3}$$

For constant c_p, and taking $h_{ref} = 0$ at T_{ref}, the above equation can be integrated to obtain the sensible heat as

$$h = c_p\,(T\text{-}T_{ref}) \tag{4}$$

In order to establish the region of phase change, the latent heat contribution was calculated from the predicted temperature field and was used to identify the regions of three phases. The nodal latent heat is a function of temperature of that specific node, i.e. $\Delta H = f(T)$.

The energy equation was applied for the entire calculation domain, including solid, liquid, and mushy regions. In this study, the nodal latent heat was assumed to be a linear function the liquid fraction that is

$$\Delta H = \Delta H_f\, f_l \tag{5}$$

where f_l is the liquid fraction. It is assumed in the present model that $f_s = (1 - f_l)$ increases linearly from zero at the liquidus temperature to 1 at the solidus temperature. Mathematically the above statement can be represented by the following expression in terms of equivalent liquid fraction f_l.

$$
f_l = \begin{cases} 1 & when & T \geq T_l, \\ \dfrac{T - T_s}{T_l - T_s} & when & T_l \geq T \geq T_s, \\ 0 & when & T \leq T_s. \end{cases} \tag{6}
$$

where T_l and T_s are the liquidus and solidus temperatures, respectively. It is to be noted here that to simplify the modeling effort; T_l and T_s were assumed constant in the present model.

The final form of the energy equation in dimensional form can be written as follows.

$$
\frac{\partial(\rho u_i h)}{\partial x_i} = \frac{\partial}{\partial x_i}\left[\left(\frac{\mu_l}{\mathrm{Pr}}\right)\frac{\partial h}{\partial x_i}\right] - \frac{\partial(\rho u_i \Delta H)}{\partial x_i} \tag{7}
$$

The last term in Eq. (7) represents the latent heat exchange rate due to the solid-liquid phase change resulting from the laminar convective flow in the melt. The flow of melt in the mushy region is quite complicated. Because of the simplicity of the Darcy law for porous media, in the current mathematical model for the mushy fluid this law was adopted [14-16]. The above equation was suitably non-dimensionalized, and its final form is listed in Table 3.

2.3.3. Non-dimensionalization of the Governing Equations and Boundary Conditions

The general form of the 3-D laminar Navier-Stokes and energy equations [Eq. (1)] and the associated boundary conditions were non-dimensionalize by the following variables as:

$$
X = \frac{x}{D}, Y = \frac{y}{D}, Z = \frac{z}{D}, U = \frac{u}{u_{in}}, V = \frac{v}{u_{in}}, W = \frac{w}{u_{in}}, P^* = \frac{P}{\rho_o u_{in}^2}, h^* = \frac{h}{\Delta H_f}, \Delta H^* = \frac{\Delta H}{\Delta H_f} \tag{8}
$$

where D, u_{in} and ΔH_f represent the hydraulic diameter of the caster, the inlet velocity and the latent heat of solidification, respectively. All the conservation equations can be expressed in a general form of a non-dimensional partial differential equation. The Cartesian-tensor form of this equation is

$$
\frac{\partial(U_i \Phi^*)}{\partial X_i} = \frac{\partial}{\partial X_i}\left(\Gamma_\Phi^* \frac{\partial \Phi^*}{\partial X_i}\right) + S_\Phi^* \qquad i = 1,2,3 \tag{9}
$$

The values of Φ^*, and the associated definition of Γ_Φ^* and s_Φ^*, for all the transport equations are listed in Table 3. The development of a general-purpose program is considerably simplified because of the casting of the governing equations in a general form.

The non-dimensional form of the boundary conditions becomes
(i) Open-top inlet

$$
U=1, \quad V=W=0, \qquad h^* = h_{in}^*, \qquad k^* = 0.01, \qquad \varepsilon^* = c_\mu (0.01)^{3/2} / 0.05 \tag{10}
$$

(ii) Free surface

$$
\frac{\partial V}{\partial X} = \frac{\partial W}{\partial X} = \frac{\partial k^*}{\partial X} = \frac{\partial \varepsilon^*}{\partial X} = \frac{\partial h^*}{\partial X} = 0 \;, \quad U=0 \tag{11}
$$

(iii) Symmetry planes

At the X-Y plane:
$$
\frac{\partial U}{\partial Z} = \frac{\partial V}{\partial Z} = \frac{\partial k^*}{\partial Z} = \frac{\partial \varepsilon^*}{\partial Z} = \frac{\partial h^*}{\partial Z} = 0, \quad W=0 \tag{12}
$$

At the X-Z plane:
$$\frac{\partial U}{\partial Y} = \frac{\partial W}{\partial Y} = \frac{\partial k^*}{\partial Y} = \frac{\partial \varepsilon^*}{\partial Y} = \frac{\partial h^*}{\partial Y} = 0, \quad V=0 \tag{13}$$

(iv) Outlet

$$\frac{\partial U}{\partial X} = \frac{\partial k^*}{\partial X} = \frac{\partial \varepsilon^*}{\partial X} = \frac{\partial h^*}{\partial X} = 0 \tag{14}$$

$$V=W=0 \tag{15}$$

(v) Moving walls

$$U=U_s= u_s/u_{in}, \quad V=W=k^*=\varepsilon^*=0, \quad \frac{\partial h^*}{\partial Y} = \frac{\partial h^*}{\partial Z} = -\frac{\gamma D}{K}(h_s^* - h_a^*) \tag{16}$$

where γ is the effective heat transfer coefficient between the solid surface and the surrounding, h_s^* represents the non-dimensional sensible enthalpy at the ingot surface and h_a^* represents the non-dimensional ambient enthalpy. The values of the effective heat transfer coefficient along the length of the DC slab caster were taken from Vreeman and Incropera [17], which are given below.

Adiabatic section: $\qquad\qquad\qquad\qquad \gamma(x) = 0 \qquad\qquad (0 \le x < 60 \text{ mm})$ (17)

Mold-metal contact region: $\qquad\qquad\qquad \gamma(x) = 3.0 \qquad\qquad (60 \le x < 90 \text{ mm})$ (18)

Secondary cooling zone:
(a) impingement zone: $\qquad\qquad\qquad \gamma(x) = 20.0 \qquad\qquad (90 \le x < 100 \text{ mm})$ (19)

(b) water streaming zone:

$$\gamma(x) = \gamma_{max} + \frac{x - x_2}{x_3 - x_2}(\gamma_{film} - \gamma_{max}) \qquad (100 \le x < 140 \text{ mm}) \tag{20}$$

$$\gamma(x) = \gamma_{film} \qquad\qquad (x \ge 140 \text{ mm}) \tag{21}$$

where $x_2 = 100$, $x_3 = 140$ mm and $\gamma_{max} = 20.0 \ kW/m^2K$, $\gamma_{flim} = 10.0 \ kW/m^2K$.

It is to be noted here that for the mold, impingement and streaming zones, three different cooling water temperatures, namely 10, 20 and 30°C, respectively, have been invoked to model the slab casting process for maintaining the consistency with the industrial low-head DC casting operations [18].

Table 3. Summary of the non-dimensional governing equations.

Equation	Φ^*	Γ_Φ^*	S_Φ^*
Continuity	1	0	0
U-momentum	U	$\dfrac{1}{\text{Re}}$	$-\dfrac{\partial P^*}{\partial X} + \dfrac{\partial}{\partial X_i}\left(\Gamma_\Phi^* \dfrac{\partial U}{\partial X_i}\right) - \dfrac{A^*}{\text{Re}}(U - U_s) - \dfrac{Gr_m}{\text{Re}^2}\left(h^* - h_\alpha^*\right)$
V-momentum	V	$\dfrac{1}{\text{Re}}$	$-\dfrac{\partial P^*}{\partial Y} + \dfrac{\partial}{\partial X_i}\left(\Gamma_\Phi^* \dfrac{\partial V}{\partial X_i}\right) - \dfrac{A^*}{\text{Re}}(V - V_s)$

W-momentum	W	$\dfrac{1}{\text{Re}}$	$-\dfrac{\partial P^*}{\partial Z} + \dfrac{\partial}{\partial X_i}\left(\Gamma_\Phi^* \dfrac{\partial W}{\partial X_i} \right) - \dfrac{A^*}{\text{Re}}\left(W - W_s \right)$
Energy	h^*	$\dfrac{1}{\text{Re}\times\text{Pr}}$	$-\left(\dfrac{\partial U\Delta H^*}{\partial X} + \dfrac{\partial V\Delta H^*}{\partial Y} + \dfrac{\partial W\Delta H^*}{\partial Z} \right)$
where		$\text{Re} = \dfrac{\rho u_{in} D}{\mu}$; $A^* = \dfrac{C\left(1 - f_l\right)^2}{f_l^{\,3} + q}$; $q = 1\times 10^{-30}$	

2.4. Solution Procedure and Grid Independent Tests

The governing partial differential equations were discretized to obtain their algebraic counterparts by using the control volume (CV) based finite difference technique on a staggered grid system. The convection-diffusion terms in the governing equations were discretized by employing the hybrid difference scheme [19]. The five variables of this problem, namely, U, V, W, P*, h*, were solved iteratively in a sequential manner to obtain a converged solution. To resolve the velocity-pressure coupling in the three momentum equations, the SIMPLE algorithm [19-20] was used. In the actual implementation of the SIMPLE algorithm, an iterative solution scheme was adopted by using an implicit relaxation technique to solve the discretized equations. After a number of preliminary numerical simulations, the following implicit relaxation factors (α_i) were found to decrease the computational time quite significantly: $\alpha_u = 0.2$; $\alpha_v = 0.2$; $\alpha_w = 0.2$; $\alpha_{PC} = 0.1$; $\alpha_T = 0.4$. The discretized equations for each variable were declared to have converged when the sum of the residuals of all CVs for that particular variable (R_Φ) was less than 10^{-4}. The convergence criterion described above can be defined mathematically as follows.

$$R_\Phi = \sum_{all\,nodes} \left| a_p \Phi_p - \sum_{nb} a_{nb}\Phi_{nb} - b \right| \tag{22}$$

The CPU time per iteration was about 1.0 min. The computations were performed on a personal computer having a speed of 2.66 GHz and fitted with a RAM of 4 Gigabytes. For a typical case, to obtain a fully converged solution, it took about 3 days and required more than 4,000 iterations.

The grid independence tests were performed using three sets of grid systems, namely, $60\times 42\times 24$, $70\times 52\times 34$, and $80\times 62\times 44$ (x, y, z directions), respectively. Since the local surface heat flux is the most sensitive quantity with regard to the grid points, hence the local surface heat fluxes were compared for the above three grid arrangements. It was found that the local surface heat flux varied by less than 2.0 % between the coarse and fine grid systems for this laminar flow problem. The details of the predicted results along with the comparisons are provided in [14]. In order to conserve space, those results are not reported here. To optimize CPU resources with an acceptable level of accuracy and reasonable computational time, all production runs reported in this paper were performed with a grid distribution of $60\times 42\times 24$ grid points.

3. Code Validation

The present code was validated by comparing the positions of the solidification front provided by the experimental measurements of a rolling ingot by Jones et al. [21]. In Table 4, the comparison is given. It is apparent from the comparison that closer to the slab center, the predicted and

measured solidification front distances matched quite well, while further the thermocouples were away from the center and near the side wall the match is not that satisfactory. It is to be noted that Jones et al. did not provide the experimentally measured thermal boundary conditions in [21]. As a result, the employed standard thermal boundary conditions used in the model might not have been appropriate. Further details about the verifications of the code are available in [14].

Table 4. Comparison of experimentally measured and numerically predicted vertical distance of the solidification front from the top of the mold at the wide symmetry plane (z = 0) for aluminum (AA-3104) alloy.

Number of sacrificial thermocouple	Horizontal distance from the narrow face of the mold wall at the wide symmetry plane (mm)	Jones et al. expts. (mm)	Present numerical prediction (mm)	Relative percent error
1	45	63.8	140	119.4 %
2	147	191.3	281	46.89 %
3	249	418.2	382	8.66 %
4	351	568.6	510	10.31 %

4. Results and Discussion

In the present study, the casting speed was varied from 40 to 80 mm/min, the inlet-melt superheat was changed from 16 to 64°C and the imposed metal-mold contact heat transfer coefficient was considered to take three distinct values, namely 1,500, 3,000 and 4,500 W/(m^{2}K). The latter quantities are the suggested values in the literature. A total of eleven separate cases were simulated and to facilitate the discussion of the results a summary of the relevant parameters and their corresponding numerical values used in the simulations is listed in Table 5. To incorporate the natural convection effects, the modified Grashof number (Gr$_m$) which appeared in the u-momentum equation due to the implementation of the Boussinesq approximation, was considered to be 10^9, and was kept fixed in all cases. Although a quadrant of the solution domain was simulated in this study, but by mirror imaging the results of the simulated quadrant the results for the entire cross section could be easily obtained.

Table 5. values of the parameter used in open-top melt delivery arrangement.

Case	Casting speed (*mm/min*)	Inlet melt superheat (ΔT) in ($^\circ$C)	Mold-metal contact HTC W/m^2K	Reynolds number	Peclet number
(1)	40	64	3000	1169.15	25.93
(2)	60	64	3000	1753.73	38.90
(3)	80	64	3000	2338.30	51.87
(4)	60	64	1500	1753.73	38.90
(5)	80	64	1500	2338.30	51.87
(6)	60	64	4500	1753.73	38.90
(7)	80	64	4500	2338.30	51.87
(8)	60	16	3000	1753.73	38.90
(9)	80	16	3000	2338.30	51.87

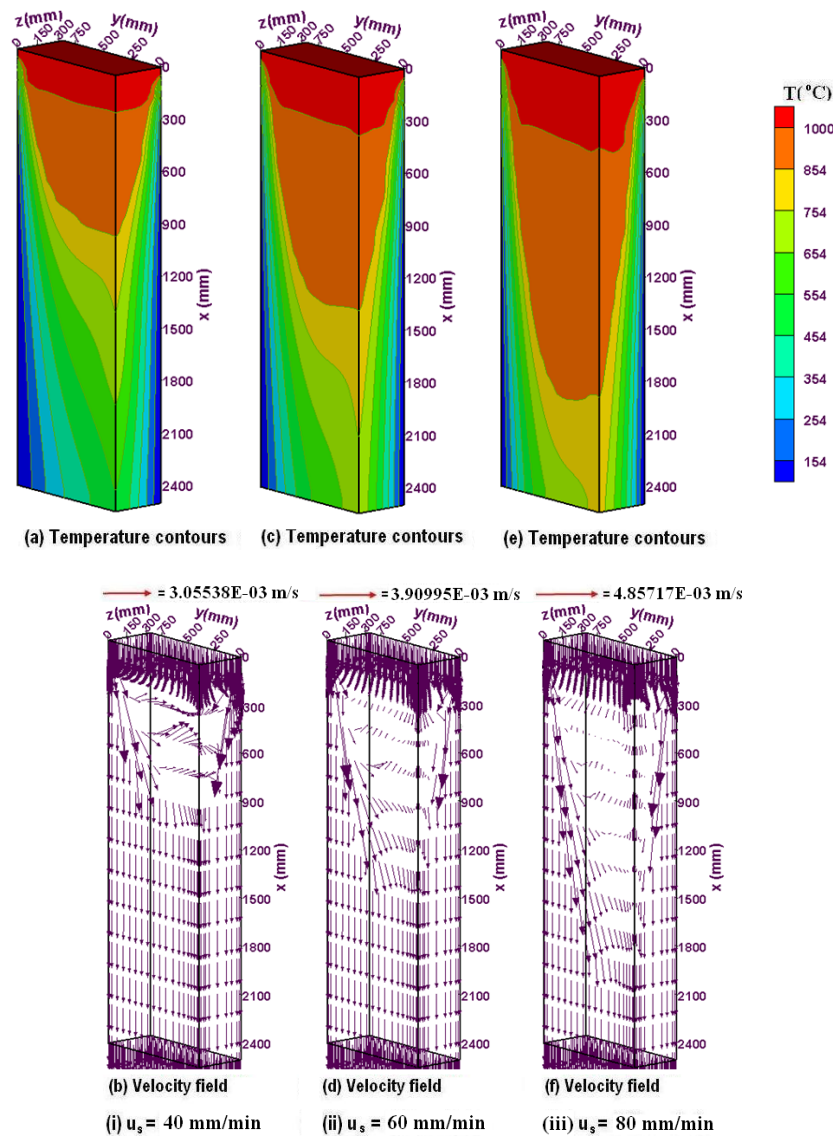| (10) | 60 | 32 | 3000 | 1753.73 | 38.90 |
| (11) | 80 | 32 | 3000 | 2338.30 | 51.87 |

Figure 2. 3-D surface plots of temperature and velocity fields for three cases (1–3).

4.1. Velocity Fields for Cases (1-3) of Table 5

Figure 2(b,d,f) shows a 3-D surface plot of the velocity vector fields on the wide (x-y plane) and the narrow (x-z plane) symmetric planes as well as the melt entry surface of the simulated caster. As stated earlier, the melt in this study is considered to have been delivered uniformly at the corresponding casting speed across the entire top cross-section. Due to this simple melt feeding system, from these figures, it can be clearly seen that all of the melt flows downward. Along the narrow and wide faces parts of the vertical melt that flow near the walls are diverted by the developed solidified shells, and then they follow the solidification fronts. An increase in the casting speed certainly increases the mass flow rate of the melt into the caster. As a consequence,

the magnitude of the resultant velocity vector increases with the increase of the casting speed. The above observation is due to the conservation of mass into the domain.

The right-hand frames of Figures 3(a-c) through Figures 5(a-c) illustrate the 2-D projections of the velocity vectors at the wide symmetry plane (z = 0) and parallel to the wide symmetry plane at two inward locations, viz., z = 62.5 mm, and z = 312.5 mm, for cases (1-3). While plotting the results about two-third of the axial domain is magnified for better visualization and clear understanding of the flow patterns prevailing within the cast. The velocity vectors in the wide symmetry plane (z = 0) for three casting speeds are portrayed in Figures 3(a) through 5(a). It should be noted that from the 3-D surface plots of the velocity vectors, one can extract the same information which are shown in the above figures.

In order to visualize what is happening in the melt for this high-temperature opaque system, the velocity fields on the longitudinal planes at an inward distance of z = 62.5 mm and z = 312.5 mm from the wide symmetry plane, are presented in Figures 3(b) through 5(b), and 3(c) through 5(c), respectively for three cases (1-3). From the velocity vector field at z = 62.5 mm it can be observed that the developing solidified shell is still obstructing the corner stream near the narrow face and this is true for all three casting speeds, but the velocity field at z = 312.5 mm, which is nearer to the rolling face shows an almost uniform downward flow. The similarity of the flow near the plane at z = 62.5 mm with a boundary layer type of flow along a moving plate is clearly visible in this plane. It is to be noted that the magnitude of the velocity vectors at z = 312.5 mm is slightly higher than the corresponding casting speed, which means that the melt is accelerated in this plane with respect to the imposed casting speed.

4.2. Temperature Fields for Cases (1-3) of Table 5

The solidification front, the liquidus isotherm along with the other iso-temperature contours are shown in Figures 2(a,c,e) for the three cases (1-3) of Table 5. The mushy region, which is bounded by the liquidus (1000°C) and solidus (854°C) isotherms, can be clearly observed in these figures. At each casting speed, it is seen that a classical parabolic-shaped solidification front is developed which signifies a weaker thermal convection effect in the mushy region. The very strong effect of the casting speed on the temperature fields is clearly visible in the above figures. The above figures further show that the extent of the melt region within the domain is enlarged with the increasing casting speed which can be easily visible from the comparative locations of the liquidus isotherm. The solidification front as well as the other isotherms is becoming steeper and are moving in the cast, direction with the increase in the casting speed. The mushy region is also seen to be expanding due to the stronger thermal convection. It must be emphasized here that there is a lack of available information regarding effective heat transfer coefficients, and, as a result, the same values of the coefficients in the primary and secondary cooling regions were used irrespective of the casting speed. The effective heat transfer coefficients were although different from the mold, impingement, and free stream falling regions, but were kept constant for all simulated casting speeds. Because of this assumption, with the increase in the mass flow rate as well as with the accompanying decrease of the residence time of the melt with the increase of the casting speed, the ingot is not sufficiently cooled by the extraction of heat. It is also observed from these figures that at and near the central area of the ingot the solidification front has turned to almost horizontal in shape. The weak vertical melt flow at and near the central area has caused negligible thermal convection, and, as a result, the shape of the solidification front has altered. With the increase in casting speed, the horizontal extent of the solidus isotherm is decreasing. The

primary reason behind this outcome is that at a lower casting speed near the solidification front the conduction mode of heat transfer is enhanced with respect to the thermal convection.

The knowledge of the temperature profiles for this high-temperature opaque system is quite useful for the development of various types of micro models including models for hot tears, cold cracks, micro-segregation, etc. To this end, the selective temperature contours, at $z = 0$, $z = 62.5$ mm and $z = 312.5$ mm for three cases (1-3) are shown in the left-hand frames of Figures 3(a) through 5(a), 3(b) through 5(b), and 3(c) through 5(c), respectively. The rate of heat extraction increases as one proceeds from the wide symmetry plane along the narrow wall toward the wide rolling face. The shapes and locations of the isotherms at the above three longitudinal planes are the manifestations of the above fact. In comparison to the symmetry plane, the temperature contours are seen to have been lifted upward in the other two planes. From these figures, it can be further observed that both the liquidus and the solidus isotherms have moved downward with the increase of the casting speed and there is also a corresponding increase in the vertical separation distance between them.
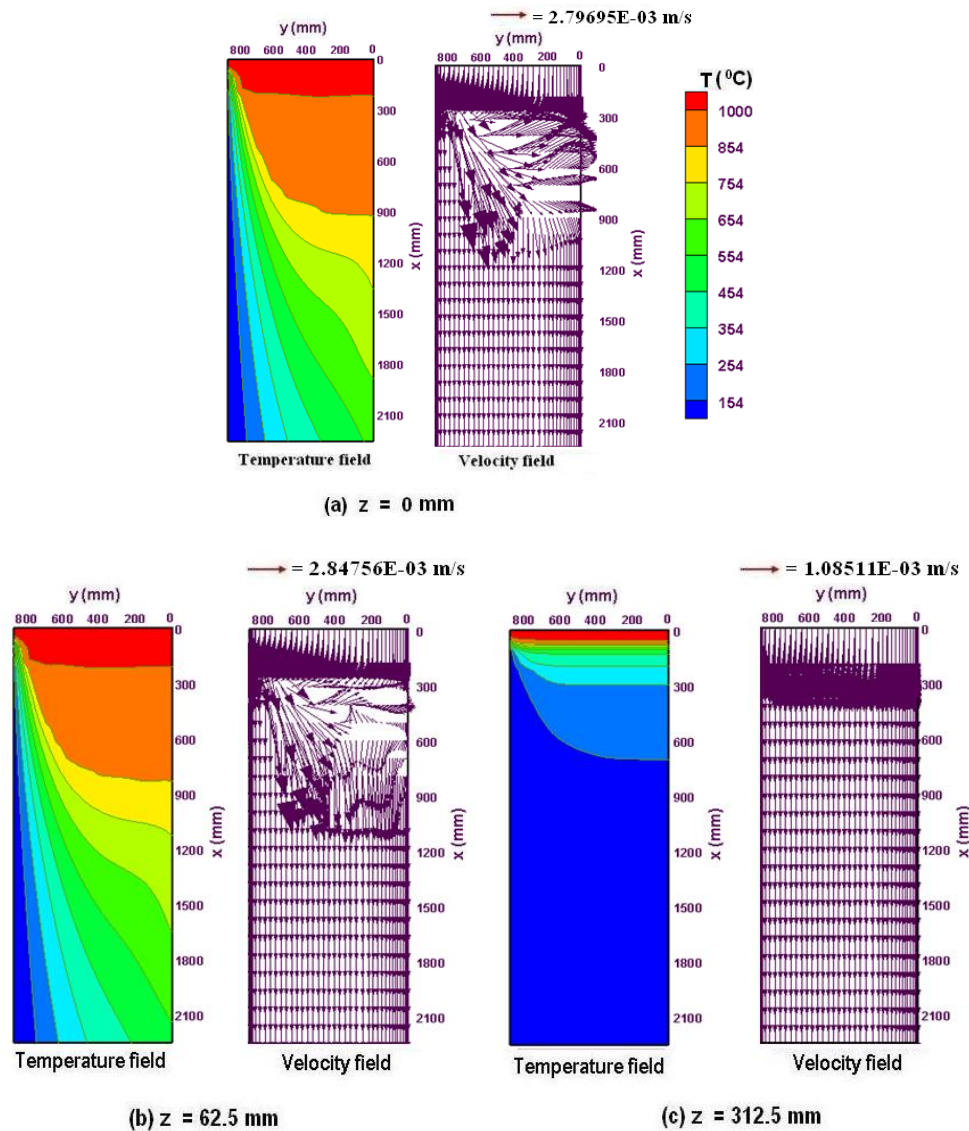

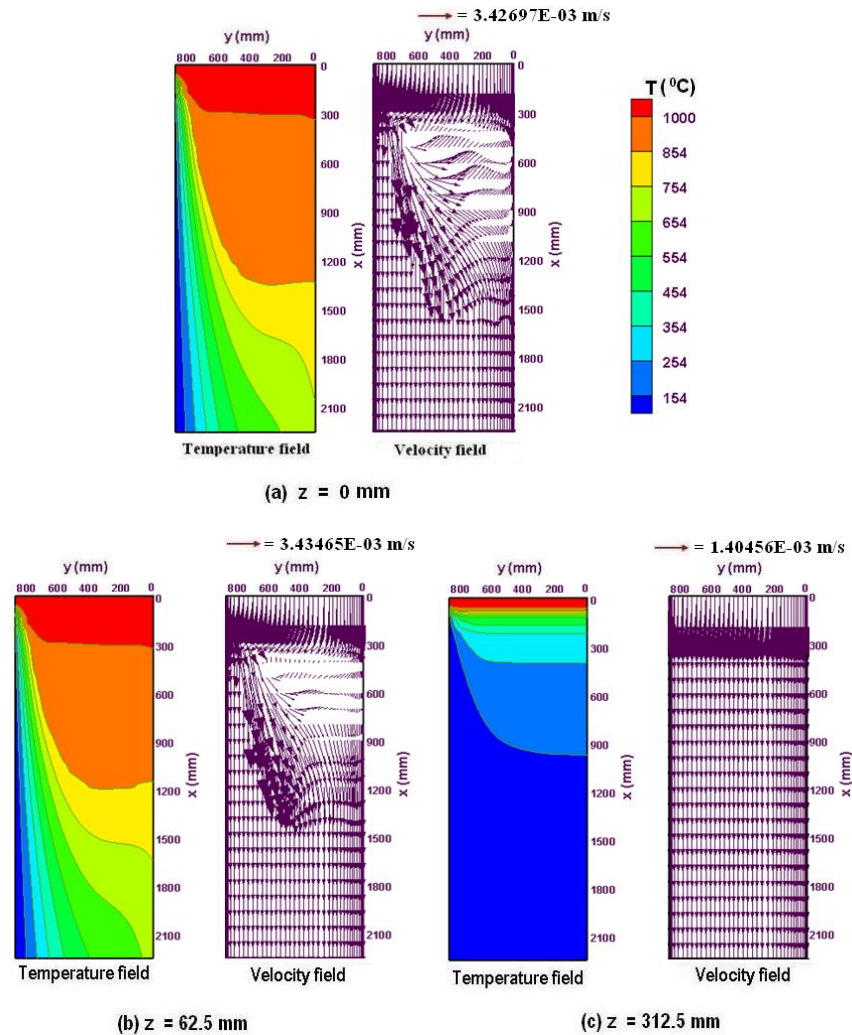Figure 3. Longitudinal 2-D views of temperature contours and velocity vectors for case 1.

Figure 4. Longitudinal 2-D views of temperature contours and velocity vectors for case 2.

Figure 6(a-c) shows the 2-D transverse cross-sectional plots along the casting direction for three cases (1-3). These figures clearly show the longitudinal developments of the solid shell and mushy zone at different cross-sections (y-z plane) parallel to the slab top surface. To get a better understanding of what is happening within the ingot in each of the above figures, a total of seven cross-sections of the ingot are depicted. With the downward movement, since more heat is being extracted from the ingot through the mold walls and by the chilled water jets, the thickness of the solid layer from the wide and narrow sides are progressively increasing which are obvious from these figures at each casting speed. Nearly uniformly thick solid shell on the narrow and wide faces convey the fact that an almost uniform rate of heat extraction is taking place from both the sides at each cross-section. Since in the corner region heat is being extracted from both the rolling and narrow faces, this has resulted in a higher rate of heat extraction there compared to the other locations and this enhanced heat transfer has caused in the almost round-shaped solid layer and mushy zone. With the increase in the casting speed, the marked reduction of the extent of the solid region along the casting direction is clearly portrayed in the above figures. The fundamental reasons for this expected outcome have already been explained in the preceding paragraph.
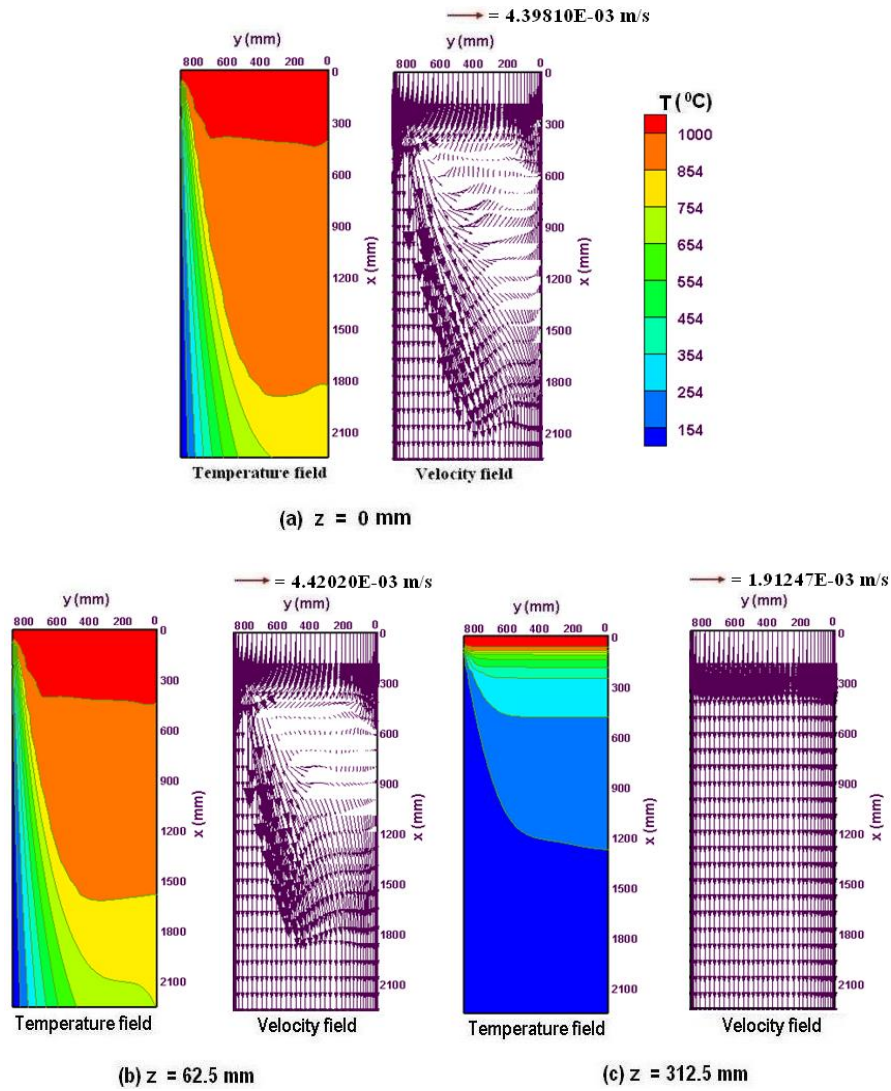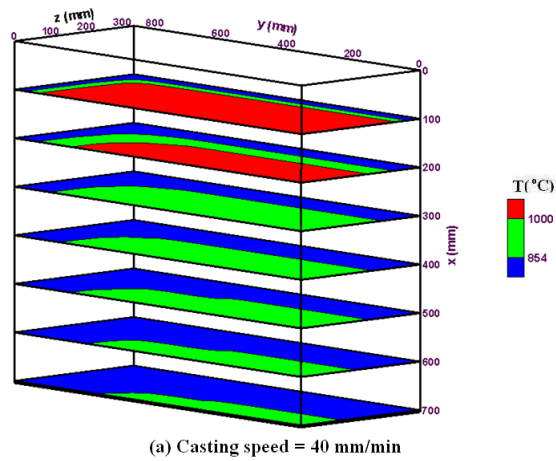
(a) z = 0 mm

(b) z = 62.5 mm

(c) z = 312.5 mm

Figure 5. Longitudinal 2-D views of temperature contours and velocity vectors for case 3.

(a) Casting speed = 40 mm/min

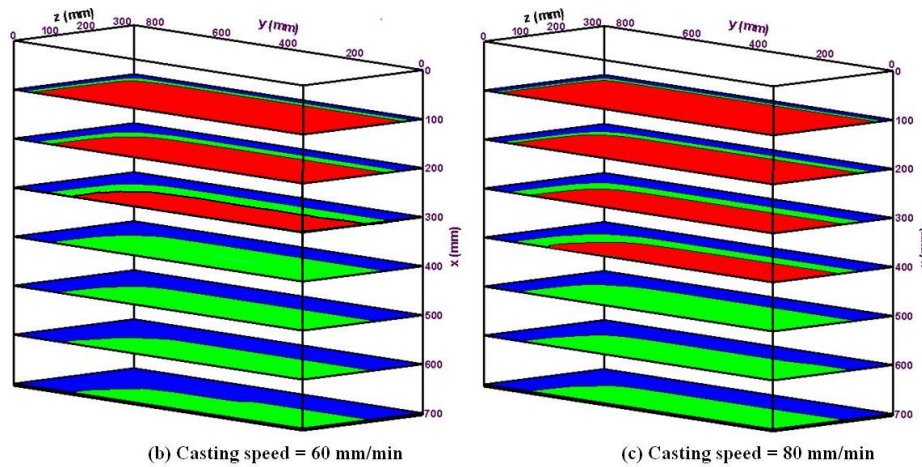(b) Casting speed = 60 mm/min   (c) Casting speed = 80 mm/min

Figure 6. Contours of solidus and liquidus temperatures at various transverse cross-sectional planes for three cases (1–3).

4.3. Quantitative Analysis for ΔT = 64ºC

4.3.1. Sump Depth and Mushy Layer Thickness

In DCC process the quality of the cast is predominantly determined by the depth of the sump and the thickness of the mushy region. The latter two quantities are very difficult to obtain through experiments during the casting operations. The mathematical model is a viable alternative for the predictions of the two said quantities. From the predicted temperature field, the above quantities are calculated through linear interpolation of the temperature with respect to the vertical distance. In Table 6, the sump depth and the mushy layer thickness at the ingot center for three cases (1-3) are given. The present authors are a bit puzzled by the fact that in none of the vast literature on DCC process for non-ferrous alloys there is any reporting of the quantitative values of the sump depth and mushy thickness.

With the increase in the casting speed, the sump and the mushy thickness are both increasing. For the comparison purposes, of the above two quantities the values of these quantities for the lowest casting speed of $40\, mm/\min$ were taken as the base case. For a withdrawal speed of $40\, mm/\min$ the sump depth is found to be approximately 841.80 mm from the top of the mold and the mushy thickness was 131.95 mm at the ingot center. In the cases for the higher casting speeds of 60, and $80\, mm/\min$, about 49.08 % and 108.58 % higher values in the sump depth were obtained, respectively. The corresponding relative increases in the mushy thickness were about 91.96 %, and 149.54 %, respectively.

Table 6. Sump depth and mushy thickness in mm at the ingot center for cases (1-3).

Quantity	Values of casting speed (u_s) in $mm/\min$		
	40	60	80
Sump depth (mm)	841.80	1254.97	1755.79
Mushy thickness (mm)	131.95	253.29	329.27

4.3.2. Predicted Shell Thickness

The casting speed increases the productivity of the DCC process. It is the aim of all slab producers to produce high-quality casts at higher casting speeds and with larger cross-sections. But in reality, the above two quantities can't be arbitrarily increased since various internal and surface defects appear in the cast if prior study and planning of the above two aspects are not carefully thought out. In this regard, fruitful guidance can be obtained from the equivalent industrial practices or through the study of the relevant literature.

Casting speed is the predominant controlling parameter that determines the magnitude of the shell thickness. As mentioned in the introduction, the breakout or run-out condition must be avoided at all cost in a DCC process. For this reason, the shell thickness at the exit of the mold is a crucial quantity. The predicted shell thickness from the narrow side of the wide symmetry plane and from the wide side of the narrow symmetry plane at the exit of the mold representing an axial distance of 90 mm from the top free surface is given in the form of bar charts for three casting speeds for three cases (1-3) in Figure 7. The numerical value inside each bar of the chart of this figure shows the predicted value of the shell thickness (in mm) for three casting speeds. For both locations with the increase of the casting speed the shell thickness decreases. The rate of decrease of the shell thickness is smaller for the lower casting speeds ($\leq 60\,mm/\min$) compared to the higher casting speeds ($> 60\,mm/\min$). On examination of this figure, it is revealed that the growth rate of the solid shell at the center of the narrow side is relatively greater compared to the center of the rolling face for cases (1-3). The reason for this unequal growth rate of the shell at the mold exit is due to the proximity of the middle of the narrow side from the slab corner (region of high heat extraction) compared to the middle of the wide slab side.
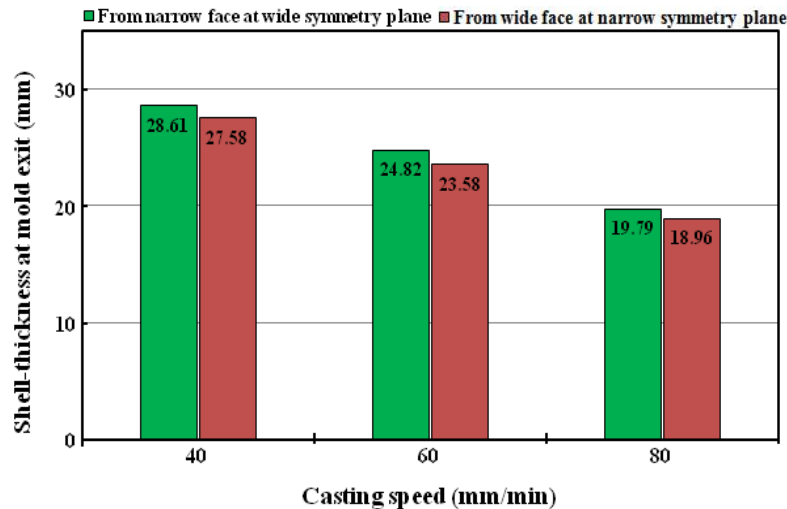

Figure 7. Shell thickness at the middle of the slab faces at mold exit vs. casting speed for cases (1–3).

4.3.3. Predicted Strand Surface Temperature

The ingot surface temperature is another important quantity to slab producers for controlling various defects. Proper imposition of the cooling conditions at the boundaries is very important to slab producers since for a specific alloy in a DCC process several physical and geometrical parameters plays complex roles, and, as a result, the surface temperatures cannot be predicted in advance without resorting to measurements or numerical predictions. There is very little

information in the literature on the trend of the heat extraction rate from the ingot surface at different operating conditions. Knowing this trend one can presumably determine where the improvements in terms of heat extraction rates are needed to obtain a good quality cast. For this reason, in this study, the ingot surface temperatures are predicted for various practical, effective heat transfer coefficients. This quantitative information may provide useful guidance in locating possible hot tears and cracking zones. It is to be recognized that the surface temperature is an unknown initially and once the converged solutions were obtained the surface temperatures were obtained by making a heat balance on each of the control volumes at the slab surface. The temperature distributions along the caster for two cases (2 and 3) are portrayed in Figures 8(a) and 8(b) corresponding to the casting speed of 60 and 80 $mm/\min$, respectively. The locations in the ingot used for the presentation of the predicted temperatures are given at the top of the above figures. Four locations are selected in this study, which are prone to the higher compressive and tensile stresses. As the effective heat transfer coefficients are increased from the mold to the sub-mold regions, the increasing rate of heat extractions decreases the temperatures significantly at the four locations, namely: (a) center; (b) mid-distance of the wide face; (c) mid-distance of the narrow face; and (d) corner point of the caster. Both figures show that from the top of the mold to the impingement point the temperature drops quite sharply and after the impingement zone the temperature drop is rather gradual except for the temperatures in the ingot central region. The midpoint of the wide face shows a slightly higher temperature compared to the midpoint of the narrow face. As a consequence of this effect, approximately 1.04 to 1.05 times thicker solid shell is seen to develop at the midpoint of the narrow face compared to the midpoint of the wide face (refer to Figure 7). The surface temperature at the corner drops more sharply and attains lower values compared to the mid-faces. The reason behind this has already been explained earlier.

This overcooled situation on the corner compared to the mid-face regions and little bit overheated situation of the wide face compared to the narrow face resulted in the unequal increase in temperatures across the ingot cross-section. This may lead to the formation of the surface and shape defects. Since the heat transfer rate from the ingot center is the lowest, hence the temperatures are the highest therein with regard to the other three locations. Within the mold and for part of the sub-mold region, the temperature at the center drops rather gradually and at a much slower rate compared to the film boiling zones in the lower part of the sub-mold region. In the latter region, the temperature drops comparatively at a higher rate until the end of the cast.

For the same axial locations, it is seen that for a higher casting speed the surface temperatures are higher compared to the lower casting speed which is clearly evident from Figures 8(a) and 8(b). The above-stated trends have prevailed in all the four ingot locations. It is to be mentioned here that irrespective of the casting speed the same convective heat transfer boundary conditions were implemented on the ingot surface without considering the enhanced cooling requirements for a higher casting speed. As a result, at the mold exit for a casting speed of 60 mm/min the ingot surface temperatures at the mid-distance of the wide and narrow faces are seen to reach approximately to 370.6, and 367.4, respectively, whereas for a casting speed of 80 mm/min their reach to a higher value of around $414.1^{o}C$ and $412.1^{o}C$, respectively. The surface temperatures for both cases show that the temperatures there are not within the nucleate boiling regime (which is below $150\,^{o}C$) and hence there could be the possibility of hot tears in those regions.

From this study, one can ascertain how to adjust the water cooling conditions in the mold and sub-mold regions so that the nucleate boiling of water, which is known to occur in a range of surface temperatures between 100 and $150\,^{o}C$ [1, 9], prevails near the exit of the mold and down

the water streaming region. If the nucleate boiling temperature range can be maintained in the sub-mold region, a high heat extraction rate from the slab surface to the cooling water can be expected there.

(a) Casting speed = 60 mm/min
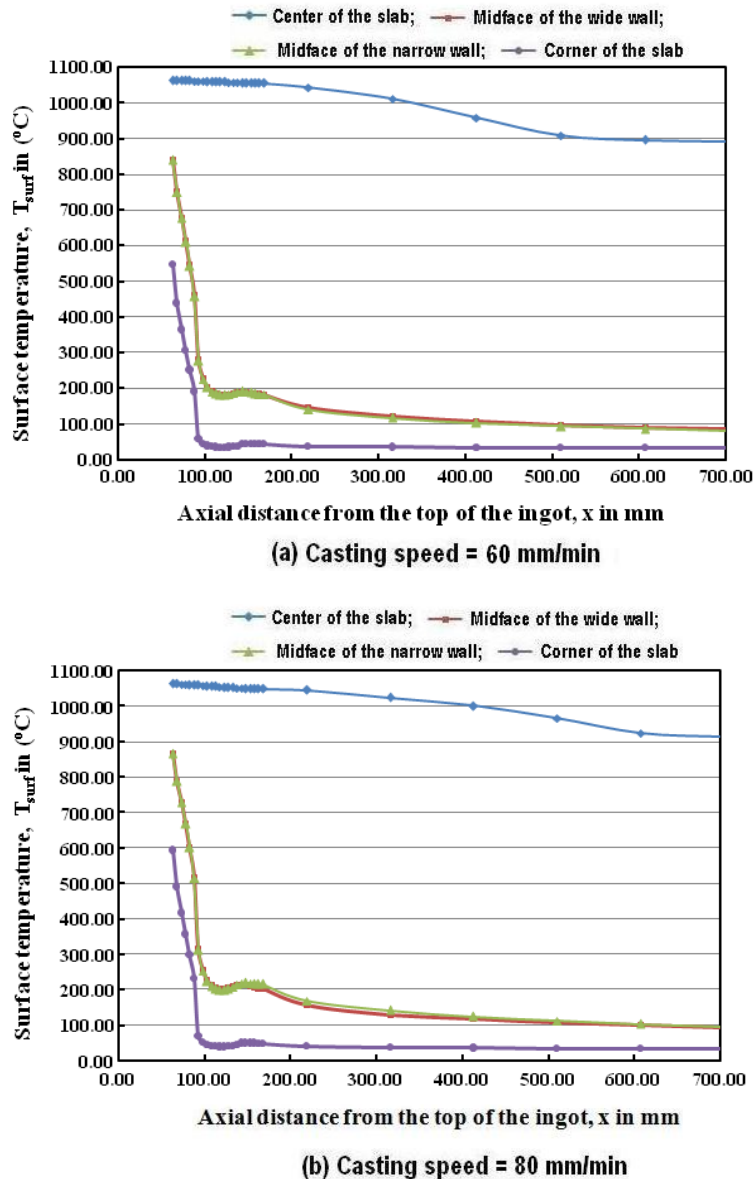

(b) Casting speed = 80 mm/min

Figure 8. Variations of surface temperature along the axial direction of the strand at four locations of the caster for: (a) $u_s = 60$ mm/min (case-2) (b) $u_s = 80$ mm/min (case-3).

4.4. Effect of Primary Coolant Heat Transfer Coefficient

The heat extraction rate through the mold not only depends on the imposed thermal boundary conditions during casting, it also depends on the melt temperature, the casting speed, the thermo-physical properties of the alloy, etc. In the case of an LH mold, it has been reported that the melt remains in contact with the mold walls up to the total length of approximately 30 mm and an air gap does not form between the solid shell and the mold walls because of the lower length of the mold compared to the conventional DC molds. There is a controversy among the researchers

working in this field regarding the values of the effective heat transfer coefficients in the mold region. From the literature, one gets conflicting values of the HTCs in the metal-mold contact region. The very well cited literature on this above issue has reported a wide range of values for the HTCs in this regard. In the metal-mold contact region, the value of HTC ranging from 1000 to 5000 W/(m²K) has been reported in the literature [1, 22]. In order to ascertain the impact of the heat transfer coefficient (HTC) at the mold-metal contact region, for an inlet superheat of 64°C, three HTCs namely 1,500, 3,000 and 4,500 W/(m²K) were selected for the two casting speeds namely, 60 and 80 mm/min.

The values of shell thickness at the mold exit for the above mentioned two casting speeds are given in the form of bar charts against the HTCs in Figure 9. The reported shell thickness is obtained through the interpolation of the temperature profile at an axial distance of 90 mm from the top inlet along the wide symmetry plane from the middle of the narrow face.
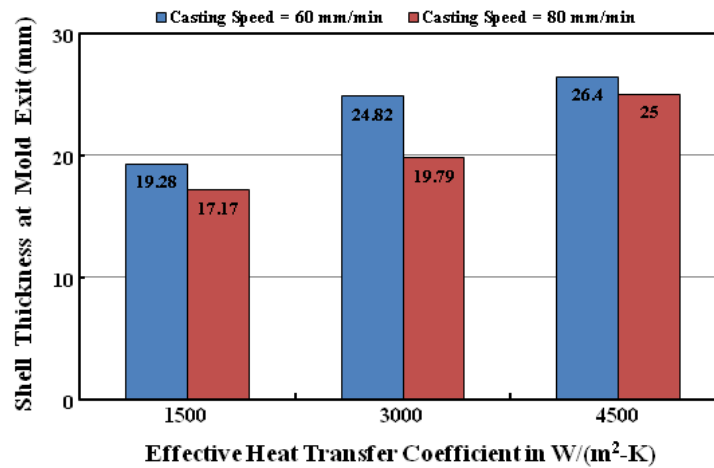

Figure 9. Shell thickness at the middle of the narrow face at mold exit vs. effective HTC (W/m²K) for six cases (2, 3, and 4-7).

With the increase of the imposed HTCs, the quantitative values of the shell thickness increase. For both casting speeds, a similar is found. As mentioned earlier with the increase of the casting speed, but for a fixed HTC, the shell thickness decreases. For the increase of HTC from 1,500 to 3,000 W/(m²K) and the lower casting speed of 60 mm/min, an enhancement of 28.73% in solid-shell thickness is found. On the contrary, for the increase of HTC from 3,000 to 4,500 W/(m²K), the increment is only 6.37%. The corresponding increase in shell thickness is about 15.60% and 26.33%, respectively, for the higher casting speed of 80 mm/min. For the lower casting speed, the effect of HTCs (from 1,500 to 3,000 W/m²K) on shell thickness is more pronounced for this alloy. From the quantitative analysis of the shell thickness, it can be concluded that the value of HTC at the metal-mold contact region has a significant effect on the shell thickness at the exit of the mold. In an industrial setting, the cooling water flow rate and its temperature in the mold should be carefully controlled such that the desired shell thickness at the exit of the mold is attained. If a solid shell of sufficient thickness at the exit of the mold cannot be obtained from using an inappropriate mold cooling condition a catastrophic breakout condition may occur.

4.5. The Effect of Inlet Melt Superheat (ΔT) on Shell Thickness

The inlet superheat of the melt is a critical issue which is usually decided by the cast operator from their previous experience of the casting campaign for an alloy. If the superheat is too low, the melt may partially solidify in the launder-trough assembly due to inevitable heat losses from the high-temperature melt to relatively cold ambient air. In such circumstances, the casting process may have to be stopped and unwanted solid needs to be removed before the next casting campaign. On the contrary, if the melt superheats is too high unwanted inter-metallic compounds may form which will inevitably deteriorate the quality of the final cast product. Another more serious problem may arise for a higher melt superheat is that a sufficiently thick solid shell may not be developed at the exit of the mold which may lead to the catastrophic breakout condition. A parametric study is carried out for three superheats, namely 16, 32 and 64°C for each of the two casting speeds of 60 and 80 mm/min. The impact of the three studied superheat is shown through the values of the shell thickness along the wide symmetry plane from the middle of the narrow face at the exit of the mold in the form of a bar chart in Figure 10. From the above figure, it is seen that with the increase of the superheat the value of the shell thickness decreases as expected. The latter statement is true for both casting speeds. In the case of the lower casting speed of 60 mm/min an increase of the superheat from 16 to 32°C has resulted in the decrease of the shell thickness of about 4.29%, whereas for the change in superheat from 32 to 64°C the reduction of shell thickness is lower which is only about 2.36%. The corresponding decrease in shell thickness with the increase in HTC is approximately 1.27% and 11.89%, respectively, for the higher casting speed of 80 mm/min. From this predicted results, it is evident that for this specific copper alloy the superheat within the range of 32 to 64°C adversely affect the solidification process for the higher casting speed.
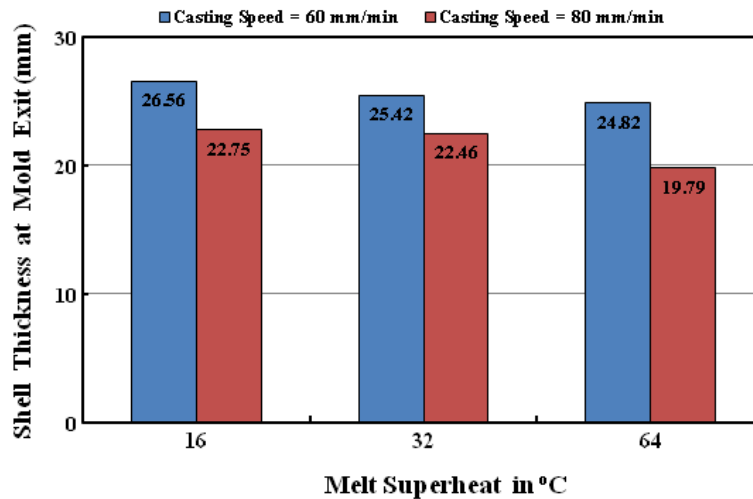

Figure 10. Shell thickness at the middle of the narrow face at mold exit vs. melt superheat (°C) for six cases (2, 3, and 8-11).

5. Conclusions

The present computational study has employed an in-house 3-D CFD code to model a DC casting process. Specifically, this study is concerned with a low-head vertical DC slab casting process for tin bronze alloy. From this study, the following conclusions can be drawn

1. The higher casting speed results in a deeper sump compared to the lower casting speed. The sump depth (SD in mm) and liquid pool depth (MD in mm) at the center for three cases (1-3) of Table 5 can be represented as a function of the simulated casting speed (u_s in mm/min) by the following linear equations, respectively: $SD = -86.798 + 22.850\ u_s\ (R^2 = 0.997)$ and $MD = -28.988 + 17.917\ u_s\ (R^2 = 0.989)$.

2. The vertical extent of the mushy region, which is bounded by the liquidus temperature of $1000^{o}C$ and solidus temperature of $854^{o}C$ of the simulated tin bronze alloy, shows that at the ingot center it increases with the increase in the casting speed in a linear fashion. The mushy thickness at the center (MT in mm) for three cases (1-3) of Table 5 can be represented as a function of the casting speed (u_s in mm/min) by the equation: $MT = -57.810 + 4.933\ u_s\ (R^2 = 0.983)$.

3. For an increase in casting speed the solid shell thickness at the exit of the mold decreases, which in turn is manifested by the increase of the surface temperature of the strand. The shell thickness at the center of the narrow face at the mold exit (ST in mm) for three cases (1-3) of Table 5 can be represented by a linear function of the casting speed (u_s in mm/min) according to: $ST = 37.637 - 0.221\ u_s\ (R^2 = 0.993)$.

4. Provided all conditions remain the same, for an increase of the melt superheat, the shell thickness at the mold exit decreases and a reduction in shell thickness is more pronounced for the higher range of the superheat for the higher casting speeds.

5. When all other parameters are fixed, for a higher HTC at the metal-mold contact region, the shell thickness at the mold exit is greater. The enhancement of the shell thickness is more pronounced for the lower HTCs at lower casting speed.

6. The thermal buoyancy force has a significant effect on the results. For a higher casting speed, a stronger thermal convective flow in the melt is seen to develop compared to the lower casting speed.

The above-predicted results are the first of its kind for an industrial scale slab DCC of the tin bronze alloy. The present authors believe that the quantitative information provided here for various important quantities like shell thickness, sump depth, liquid pool depth, mushy thickness, etc. will help the designers and operators of such casters in a significant way

One of the difficulties encountered in modeling the mushy zone is the lack of information for the above alloy showing the functional variation of the liberation of the latent heat of solidification with temperature. In order to develop a model it is easy to allow a linear variation of liquid fraction with regard to the solidus and liquidus temperatures in the mushy zone. It is to be noted that the solidification rate in a DC casting process is rather low and hence unlike rapid solidification processes an equilibrium assumption is fully justified for this process.

Acknowledgments

References

[1] J.F. Grandfield, D.G. Eskin and I. Bainbridge, Direct-Chill Casting of Light Alloys: Science and Technology, Hoboken, Nj: John Wiley and Sons, Inc. p. 242; p. 334, 2013.

[2] D.G. Eskin, Physical Metallurgy of Direct Chill Casting of Aluminum Alloys, Advances in Metallic Alloys. Boca Raton, FL:CRC Press, Taylor & Francis Group, p. 120-122, 2008.

[3] L. Begum and M. Hasan, 3-D CFD simulation of a vertical direct chill slab caster with a submerged nozzle and a porous filter delivery system, Int. J. Heat & Mass Transfer, vol. 73, pp. 42-58, 2014.

[4] L. Begum and M. Hasan, A numerical study of 3D turbulent melt flow and solidification in a direct chill slab caster with a porous combo bag melt distributor, Numerical Heat Transfer, Part A: Applications, vol. 67(7), pp. 746-770, 2015.

[5] M. Hasan and L. Begum, Three-dimensional numerical study of a low head direct chill slab caster for aluminum alloy AA-5052, ASME Journal of Thermal Sciences and Engineering Applications, vol. 7, Article no. 021008, pp. 1-15, 2015.

[6] L. Begum and M. Hasan, A numerical study of 3D turbulent melt flow and solidification in a Direct Chill slab caster with an open-top melt feeding system, Numerical Heat Transfer, Part A: Applications, vol. 67(7), pp. 719-745, 2015.

[7] L. Begum and M. Hasan, Numerical study of turbulent flow and solidification of a Direct Chill caster fitted with a channel bag, Heat and Mass Transfer Journal, vol. 51, pp. 759-779, 2015.

[8] M. Hasan and L. Begum, Modeling of transport phenomena in low-head Direct Chill caster for AA7050 alloy, AIAA Journal of Thermophysics and Heat Transfer, vol. 30(1), pp. 168-181, 2016.

[9] J. Sengupta, B.G. Thomas and M.A. Wells, The use of water cooling during the continuous casting of steel and aluminum alloys, Metall. Mater. Trans. A, vol. 36A, pp.187-204, 2005.

[10] B. Rinderer, P. Austen and A. Tuff, Casthouse modifications for improved slab quality, Light Metals, The Minerals, Metals & Materials Society, Warrendale, PA, pp. 1-6, 2003.

[11] Tin Bronze Alloy (C903); Physical Properties, Thermal Properties. [1]www.morganbronze.com/pdf/c903_tin_bronze.pdf and [2]www.beartechalloys.com/cast-alloys-c903.html

[12] M. Hasan and L. Begum, On numerical modeling of low-head direct chill ingot caster for magnesium alloy AZ31, Journal of Magnesium and Alloys, vol. 2, pp. 275-286, 2014.

[13] M. Hasan and L. Begum, Semi-continuous casting of magnesium alloy AZ91 using a filtered melt delivery system, Journal of Magnesium and Alloys, vol. 3(4), pp. 283-301, 2015.

[14] L. Begum, 3-D Transport Phenomena in Vertical Direct Chill Casting Processes (PhD. thesis), Dept. of Mining and Materials Engineering, McGill University, Montreal, Quebec, Canada, 2013.

[15] V.R. Voller and C.A. Prakash, Fixed grid numerical modeling methodology for convection-diffusion mushy region phase-change problems, Int. J. Heat Mass Transfer, vol. 30(8), pp. 1709-1719, 1987.

[16] S.H. Seyedein and M. Hasan, A three-dimensional simulation of coupled turbulent flow and macroscopic solidification heat transfer for continuous slab casters, Int. J. Heat Mass Transfer, vol. 40(18), pp. 4405-4423, 1997.

[17] C.J. Vreeman and F.P. Incropera, The effect of free-floating dendrites and convection on macrosegregation in direct chill cast aluminum alloys part II: predictions for Al-Cu and Al-Mg alloys, Int. J. Heat Mass Transfer, vol. 43(5), pp. 687-704, 2000.

[18] Mr. Turina McClelland, Marketing Communications Director (2013). *Personal communication*s, http://www.Wagstaff.*com*

[19] S.V. Patankar, Numerical Heat Transfer and Fluid Flow, 1st ed., Hemisphere Publishing Corporation, NY:Taylor and Francis Group, p. 88-90; p. 126-131, 1980.

[20] H.K. Versteeg and W. Malalasekera, An Introduction to Computational Fluid Dynamics, The Finite Volume Method, 1st ed., Longman Scientific Technical, Longman Group Ltd., Essex, England, p. 142-146, 1995.

[21] W.K. Jones Jr, D. Xu, J. Evans, W.E. Williams and D.P. Cook, Effects of combo-bag geometry on the thermal history and sump profile of a 3104 DC cast ingot, Light Metals, The Minerals, Metals & Materials Society, Warrendale, PA, USA, pp. 841-845, 1999.

[22] E. Caron and M.A. Wells, Secondary cooling in the direct chill casting of magnesium alloy AZ31, Metall. Mater. Trans. B., vol. 40B(4), pp. 585-595, 2009.

Biographical information

Dr. Mainul Hasan is a tenured Associate Professor and has been teaching in the Department of Mining and Materials Engineering at McGill University, Montreal, Quebec for over 30 years., Dr. Hasan obtained his PhD degree in 1988 from the Department of Chemical Engineering at McGill University He obtained his M.Sc degree in 1981 from the Department of Chemical Engineering, University of Petroleum and Minerals (now King Fahd University of Petroleum & Minerals), Dhahran, Saudi-Arabia. He received his B.Sc. Eng degree in 1978 from the Department of Chemical Engineering, Bangladesh University of Engineering & Technology, Dhaka, Bangladesh.

For the past 30 or so years Dr. Hasan has been carrying out scientific research in the area of mathematical modeling with particular emphasis on the applications of advanced computational fluid dynamics (CFD) in metallurgical and chemical processes. Over the years, Dr. Hasan has published more than 100 articles in refereed journals, conferences proceedings and as book chapters. At McGill, he has supervised or co-supervised 12 PhD students and a host of M.Eng students. Dr. Hasan is a senior member of the American Society of Mechanical Engineers (ASME) and American Institute of Chemical Engineers (AIChE).

Dr. Latifa Begum, since September, 2017, is working as a Research Engineer in the Department of Mining and Materials Engineering, McGill University, Montreal, Quebec, Canada. From September, 2015 to August, 2017, she worked as an NSERC Post Doctoral Fellow (PDF) at Concordia University in the Department of Mechanical and Industrial Engineering, Montreal, Canada under the supervision of Prof. G. H. Vatistas. In 2008 and 2014, she obtained the M.Eng. in Materials Engineering (Thesis Option) degree and PhD in Materials Engineering degree, respectively from the Department of Mining and Materials Engineering, McGill University, Montreal, Quebec, Canada under the supervision of Professor Mainul Hasan. She obtained her Bachelor of Science (B.Sc.) in Engineering degree in 1989 and Master of Science in Engineering (thesis option) degree in 1988 from the Department of Mechanical Engineering, Bangladesh University of Engineering & Technology, Dhaka, Bangladesh. From the year 1990 to

2001, she was a government officer worked as a Mechanical Engineer in the Ministry of Communication of Bangladesh. Over the last four years, Dr. Latifa Begum published as a first or as a co-author twenty-six journal papers in various high impact factor heat and fluid flow journals and a number of conference papers. Dr. Latifa Begum has been carrying out scientific research in the area of mathematical modeling with particular emphasis on the applications of advanced computational fluid dynamics in metallurgical and energy storage/retrieval processes.